Geochemistry Geophysics Geosystems G3

Article
Volume 14, Number 7
29 July 2013
doi: 10.1002/ggge.20177
ISSN: 1525-2027

Published by AGU and the Geochemical Society

# Observations of the volume flux of a seafloor hydrothermal plume using an acoustic imaging sonar

**G. Xu**
*Institute of Marine and Coastal Sciences, Rutgers University, 71 Dudley Road, New Brunswick, New Jersey, 08901, USA (guangyu@marine.rutgers.edu)*

**D. R. Jackson**
*Applied Physics Laboratory, University of Washington, Seattle, Washington, USA*

**K. G. Bemis and P. A. Rona**
*Institute of Marine and Coastal Sciences and Department of Earth and Planetary Sciences, Rutgers University, New Brunswick, New Jersey, USA*

[2] We present a 26 day time series (October 2010) of physical properties (volume flux, flow velocity, expansion rate) of a vigorous deep-sea hydrothermal plume measured using our Cabled Observatory Vent Imaging Sonar (COVIS), which is connected to the Northeast Pacific Time Series Underwater Experiment Canada Cabled Observatory at the Main Endeavour Field on the Juan de Fuca Ridge. COVIS quantitatively monitors the initial buoyant rise of the plume from ~5 m to ~15 m above the vents. The time series exhibits temporal variations of the plume vertical volume flux ($1.93 - 5.09\ m^3/s$), centerline vertical velocity component ($0.11 - 0.24\ m/s$) and expansion rate ($0.082 - 0.21\ m/m$); these variations have major spectral peaks at semidiurnal (~2 cycle/day) and inertial oscillation (~1.5 cycle/day) frequencies. The plume expansion rate (average $\sim 0.14\ m/m$) is inversely proportional to the plume centerline vertical velocity component (coefficient of determination $R^2 \sim 0.5$). This inverse proportionality, as well as the semidiurnal frequency, indicates interaction between the plume and ambient ocean currents consistent with an entrainment of ambient seawater that increases with the magnitude of ambient currents. The inertial oscillations observed in the time series provide evidence for the influence of surface storms on the dynamics of hydrothermal plumes.

**Components:** 7,495 words, 9 figures, 2 tables.

**Keywords:** hydrothermal plume; acoustic imaging; Doppler velocity; entrainment; volume flux; flow velocity.

**Index Terms:** 3000 Marine Geology: Hydrothermal systems, Instruments and techniques.

**Received** 16 November 2012; **Revised** 14 May 2013; **Accepted** 15 May 2013; **Published** 29 July 2013.

Xu, G., D. R. Jackson, K. G. Bemis, and P. A. Rona (2013), Observations of the volume flux of a seafloor hydrothermal plume using an acoustic imaging sonar, *Geochem. Geophys. Geosyst., 14,* 2369–2382, doi:10.1002/ggge.20177.

## 1. Introduction

[3] Hydrothermal plumes, occurring mainly at mid-ocean ridges, disperse the heat, chemicals, and biological materials from the vents on the seafloor [*Stein and Stein*, 1994; *Anderson and Hobart*, 1976; *Bickle and Elderfield*, 2004; *Jackson et al.*, 2010; *Adams et al.*, 2012] and induce unique patterns of deep-ocean circulations around the vent fields [*Thomson et al.*, 2003, 2005].

© 2013. American Geophysical Union. All Rights Reserved.

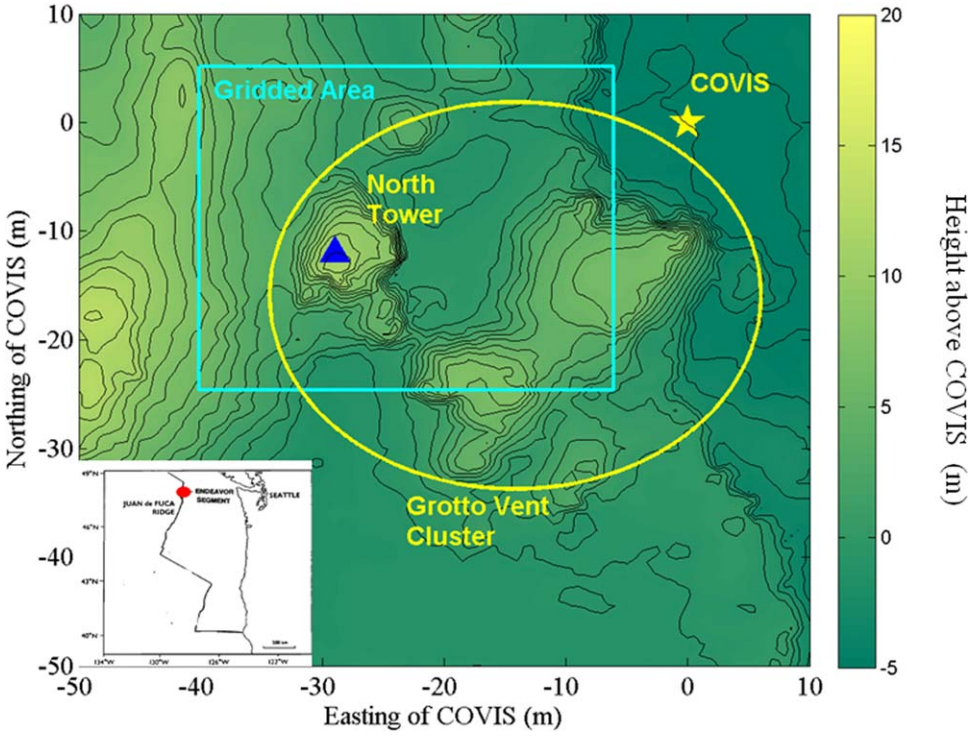


**Figure 1.** Bathymetry relative to COVIS (yellow star) around the Grotto mound (yellow ellipse) with contours in 1 m intervals. The blue triangle denotes the location of the North Tower; the light blue rectangle defines the horizontal cross-section area of the 3-D grid. (bottom left) Index map: the Juan de Fuca ridge and the Endeavour segment (red dot)

Traditional hydrothermal-vent studies have depended on ship and submersible-based experiments or moored self-contained instruments to collect data that are mostly snapshots or intermittent time series with limited durations [*Bemis et al.*, 1993; *Rona and Trivett*, 1992; *Kellogg and McDuff*, 2010; *Larson et al.*, 2007; *Crone et al.*, 2010; *Xu and DiIorio*, 2012]. These data are insufficient to resolve the interaction of a hydrothermal system with the geological changes of a mid-ocean ridge and the hydrodynamic influences of the deep-ocean currents, both of which require long-term continuous time-series measurements of the plume properties of interest (i.e., temperature, chemical concentration, volume flux, and flow rate).

[4] In September 2010, the Cabled Observatory Vent Imaging Sonar (COVIS) was installed in the world's first regional-scale underwater ocean observatory network Northeast Pacific Time-Series Underwater Experiment (NEPTUNE) Canada (http://www.neptunecanada.ca). COVIS quantitatively monitors the initial buoyant rise of a plume from ~5 to ~15 m above the Grotto mound in the Main Endeavour Field (MEF) on the Juan de Fuca Ridge. This observed plume is the integrated product of multiple high-temperature black-smoker-type vents discharging from a partially isolated sulfide edifice 10 m high and 10 m in diameter at the north-western end of the Grotto mound (which we call the North Tower of Grotto hereafter, Figure 1). Powered by the NEPTUNE Canada network, COVIS scans the plume with acoustic signals and records the acoustic backscatter from the plume. Fiber optic cables of the NEPTUNE Canada network transfer the acoustic data collected by COVIS in near-real time to the Internet-based Data Management and Archival System (http://dmas.uvic.ca/home), which provides free data access to both the scientific community and the general public. The advent of NEPTUNE Canada and COVIS enables researchers to monitor hydrothermal plumes in real time for long time periods (up to years), which is beyond the capabilities of traditional vent studies, and thus understand the plumes' interactions with geological and hydrodynamical mechanisms.

[5] In this study, with a Doppler analysis of the acoustic data collected by COVIS, we present a 26 day time series of the plume's volume flux,

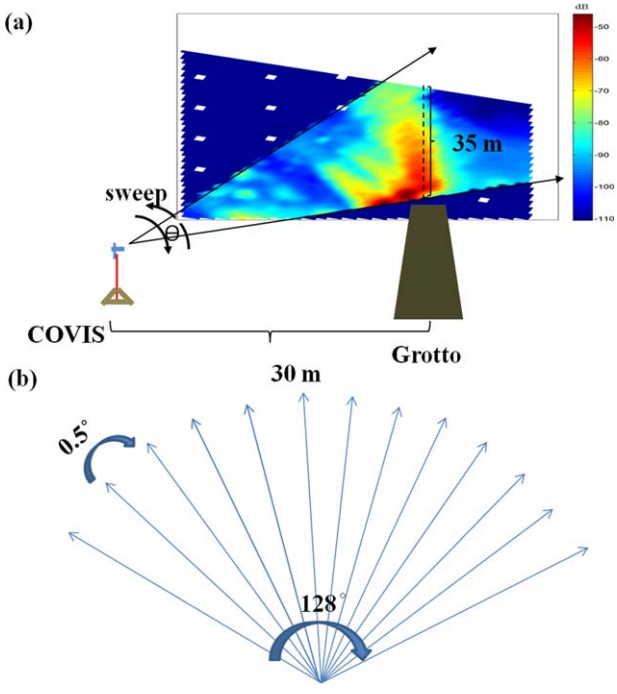


**Figure 2.** Configuration of COVIS data acquisition. (a) Vertical cross section of a standard COVIS 3-D plume image. (b) Fan-shape beam pattern at each elevation angle $\theta$.

centerline vertical flow rate, and expansion rate sampled at 3 h intervals. The temporal variations observed in the time series provide insight into the interaction of the plume with both the tidal oscillations in the surrounding deep-ocean currents and the surface wind-driven inertial oscillations. Section 2 is an introduction to the sonar configuration and data acquisition of COVIS, the data-processing method used to obtain the time series, and the quantification of the measurement uncertainty. Section 3 summarizes the important observations in the time series. Section 4 discusses the advances in COVIS data collection and explains the potential causes of the observed temporal variations in the time series. Section 5 includes concluding remarks.

## 2. Methods

### 2.1. Acoustic Data Collection

[6] COVIS was deployed at $47^\circ 57'\mathrm{N}, 129^\circ 6'\mathrm{W}$, approximately 30 m to the northeast of the North Tower of Grotto, and 2197 m depth looking in the southwest direction (Figure 1). Power and data connectivity are supplied to COVIS through its connection to the Endeavour node of the NEPTUNE Canada cabled observatory. COVIS takes samples every 3 h in three different modes (imaging, Doppler and diffuse flow) for 3-D plume imaging, volume flux quantification, and 2-D imaging of diffuse flows. This paper deals with the Doppler mode only.

[7] The primary component of COVIS is a state-of-the-art imaging sonar, a variant of the Seabat 7125 developed by Reson, Inc. The 400 kHz transmitting-receiving pair provides angular coverage of $128^\circ$ (horizontal) $\times 1^\circ$ (vertical) with 256 beams at a resolution of $0.5^\circ \times 1^\circ$. The 200 kHz pair is used for diffuse flow measurements, which are outside the scope of this paper. Figure 2 is a schematic plot of the acoustic data acquisition method. During one scanning cycle, the sonar first rotates upward from elevation angle $\theta = 20^\circ$ to $57^\circ$ in $1^\circ$ increments and then downward in $1^\circ$ increments to the initial position. The combination of the upward and downward rotation processes is called a sweep, which covers a vertical range of 35 m of the plume. At each $1^\circ$ elevation angle, COVIS transmits 40 pulses (pings) (20 pulses each during the upward and downward halves of a total sweep at each $1^\circ$ elevation angle) of high-frequency (396 kHz) acoustic signals with the ping rate $\sim$5 Hz toward the plume atop the North Tower of Grotto. Multiple transmissions (to be averaged), data acquisition and storage, and mechanical rotation of the sonar (with instantaneous rotation speed $\sim 1^\circ/\mathrm{s}$) result in a combined upward and downward rotation (a total sweep) time of 23 min. Two consecutive sweeps are executed with 3 h intervals between each pair. Table 1 summarizes important sonar specifications.

[8] The spatial resolution along the acoustic line-of-sight is $R_r = \frac{c\tau}{2} \approx 1$ m, where $c = 1495\,\mathrm{m/s}$ is the sound speed and $\tau = 1.5\,\mathrm{ms}$ is the pulse length. Applying a conventional beam-forming technique, 256 beams are formed with azimuthal angles from $-64^\circ$ to $64^\circ$, which comprises a $128^\circ$

**Table 1.** COVIS Doppler-Mode Settings

| | | | |
|---|---|---|---|
| Central frequency | 396 kHz | Azimuthal coverage | $128^\circ$ |
| Pulse length ($\tau$) | 1.5 ms | Azimuthal resolution | $0.5^\circ$ |
| Sound speed ($c$) | 1495 m/s | Range of elevation angle | $20^\circ \sim 57^\circ$ |
| Max ping rate | 5 Hz | Vertical angular resolution | $1^\circ$ |
| Pings for average ($N_p$) | 40 | Spatial resolution ($R_v$) at 30 m | 0.15 $m^3$ |
| Sampling interval | 3 h | Spatial resolution ($R_v$) at 75 m | 1 $m^3$ |

wide "fan". The range of each beam extends to 75 m away from the sonar (Figure 2b). As the beams diverge, the elemental scanning volume of COVIS grows larger, causing resolution to become lower as the range increases. For example, at 30 m range from COVIS (where the North Tower of Grotto is located, Figure 2a) the azimuthal distance between two adjacent beams is $R_{az} \approx 0.3$ m; the orthogonal distance between two adjacent "fans" is $R_f \approx 0.5$ m. As a result, the elemental scanning volume is $R_v = R_f R_{az} R_r \approx 0.15$ m$^3$, which increases to $\sim$1 m$^3$ at 75 m range.

[9] The acoustic signals used for plume imaging and Doppler measurements are backscattered by the suspended particles and turbulence-induced temperature fluctuations within the plume. Although the relative importance of suspended particles and temperature fluctuations to acoustic backscatter remains to be resolved [*Xu and DiIorio*, 2011], it does not affect the results presented here, because suspended particles and temperature fluctuations have similar profiles across the plume [*Papanicolaou and List*, 1988], and thus produce similar backscatter patterns.

[10] Calibration factors are used to compute the acoustic volume backscatter cross-section $\sigma_b$ in units m$^{-1}$ (see supporting information S1). The $\sigma_b$ values are averaged over the 40 pings at each elevation angle. Taking the logarithm of $\sigma_b$ gives the volume scattering strength $VSS = 10\log_{10}(\sigma_b)$ in units dB m$^{-1}$, which is conventionally used to represent acoustic scattering intensity (the color scales in Figure 2a). In addition, COVIS estimates the plume velocity component along the acoustic line-of-sight $V_r$ from the Doppler frequency shift observed in the backscatter signals using the covariance method described in *Jackson et al*. [2003] (see supporting information S2). The "fans", each composed of 256 line-of-sight beams of $\sigma_b$ and $V_r$, at successive elevation angles are stacked together and interpolated to a uniform 3-D rectangular grid (0.5 m interval in all three coordinates). We then use the gridded $\sigma_b$ and $V_r$ to estimate the plume vertical volume flux, centerline vertical velocity component, and expansion rate.

## 2.2. Plume Vertical Flow Rate Estimation

[11] In order to estimate the plume vertical volume flux, the plume velocity component along the acoustic line-of-sight $V_r$ is converted to the plume vertical velocity component $W$ using the geometric technique developed by *Jackson et al*. [2003], which is summarized as follows.

### 2.2.1. Plume Centerline Location

[12] According to the "dominant eddy" concept [*Chu*, 1994], a plume's centerline can be defined as an axis or streamline that describes the direction of the coherent motion within the plume. Applying the method developed by *Rona et al*. [2002], we construct the centerline of the plume by connecting the local maxima on successive horizontal cross sections of the 3-D-gridded volume backscatter cross-section $\sigma_b$. Instead of searching for the absolute maxima, the locations of which are unstable due to the turbulence within the plume, we locate the local maxima by fitting a 2-D Gaussian curve to each cross section and pinpointing the peak of the Gaussian fit. The choice of a Gaussian function is motivated by both its ease of use and its traditional application to describing the distribution of plume properties (i.e., flow velocity, temperature, turbulent intensity) about the centerline of the plume [*Papanicolaou and List*, 1988]. The mathematical expression of the 2-D Gaussian curve is

$$\sigma_b(r) = \sigma_c \exp\left(-\frac{r^2}{b_\sigma^2}\right) + \sigma_a \tag{1}$$

$$r = \sqrt{(x - x_0)^2 + (y - y_0)^2} \tag{2}$$

where $\sigma_c$ is the peak value of the profile given zero background ($\sigma_a = 0$), $r$ is the radial distance from the centerline, $[x_0, y_0]$ are the coordinates of the Gaussian peak, $b_\sigma$ is the $e$-folding radius of the Gaussian profile (the distance from the peak to the point where the $\sigma_b$ decreases to $1/e$ (37%) of its peak value). Note that $b_\sigma$ will be used as a measure of the plume radius to determine the expansion rate later in the paper (section 2.3). As can be seen from Figure 3, the above Gaussian profile gives a good fit to the data. We then construct the plume centerline by fitting a cubic curve to the local $\sigma_b$ maxima on successive horizontal cross sections (Figure 4).

### 2.2.2. Geometric Conversion

[13] We convert the plume velocity component along the acoustic line-of-sight $V_r$ to the plume vertical velocity component $W$ based on the centerline location obtained using the method outlined in section 2.2.1 and relative angles between the acoustic line-of-sight, vertical and axial (tangential to the plume centerline) directions shown in Figure 5. We use symbols in bold fonts to denote vectors (i.e., velocities) and nonbold fonts for velocity magnitudes and components in this and the following sections.

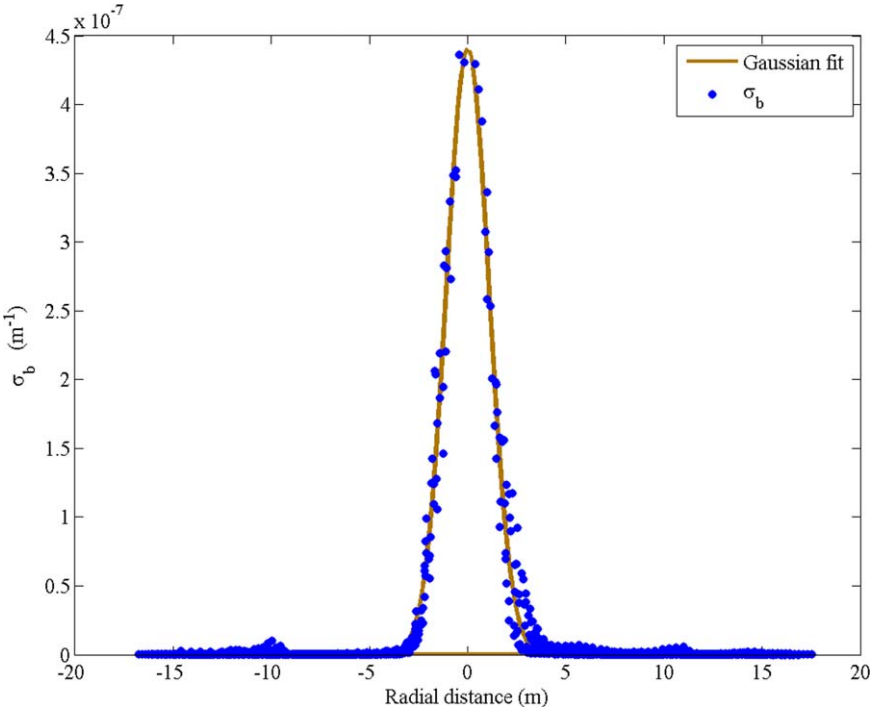


**Figure 3.** Volume backscatter cross-section $\sigma_b$ profile across a horizontal cross section at 12 m above the North Tower of Grotto and the Gaussian fit. The cross-sectional profile is extracted from the 3-D gridded $\sigma_b$ collected on 10 October 2010.

[14] The first step is to calculate the magnitude, $V_c$, of the plume velocity at a given point C on the plume centerline. By assumption, the plume centerline is also a streamline; therefore, the plume velocity at C is in the axial direction (tangential to the centerline) and thus its magnitude can be obtained using the following equation

$$V_c = \frac{V_{rc}}{\mathbf{e_c} \cdot \mathbf{e_r}} = \frac{V_{rc}}{cos(\nu)} \tag{3}$$

where $V_{rc}$ is the component of velocity along the acoustic line-of-sight at C, $\mathbf{e_c}$ is a unit vector tangent to the plume centerline, $\mathbf{e_r}$ is a unit vector pointing from the sonar to C, and $\nu$ is the angle between $\mathbf{e_c}$ and $\mathbf{e_r}$ (Figure 5). Note that $\mathbf{e_c}$ and $\mathbf{e_r}$ can be readily calculated using the plume centerline and the coordinates of C in the 3-D grid. The horizontal velocity at C is thus

$$\mathbf{V_h} = (V_c \mathbf{e_c} \cdot \mathbf{e_x})\mathbf{e_x} + (V_c \mathbf{e_c} \cdot \mathbf{e_y})\mathbf{e_y} \tag{4}$$

where $\mathbf{e_x}$ and $\mathbf{e_y}$ are unit vectors in the x and y directions.

[15] The horizontal flow field within the plume is a combination of ambient horizontal cross flows ($\mathbf{U_a}$) and entrainment inflows ($\mathbf{U_e}$). We assume $\mathbf{U_a}$ does not vary in time during each sweep (~23 min) and only varies in the vertical direction at any given moment; that is, for a given dataset (time step), $\mathbf{U_a}$ only varies vertically and is constant along each horizontal plane. We also neglect the contribution made by $\mathbf{U_e}$ (see section 2.4 for the justification of this assumption). With these assumptions, the horizontal flow field inside the plume simply equals $\mathbf{U_a}$, and thus $\mathbf{V_h}$ can be used as a proxy of the ambient horizontal flows near Grotto.

[16] The next step is to calculate the plume velocity component in the vertical direction $W_p$ at any given point P at the same altitude as the centerline point C using the line-of-sight velocity component $V_{rp}$ measured at P and the horizontal velocity $\mathbf{V_h}$ obtained in the first step. The equation applied is

$$W_p = \frac{V_{rp} - \mathbf{V_h} \cdot \mathbf{e_{rp}}}{\sin(\theta)}, \tag{5}$$

in which the numerator eliminates the contribution of $\mathbf{V_h}$ to $V_{rp}$, where $\mathbf{e_{rp}}$ is the unit vector pointing from the sonar to P and $\theta$ is the angle between $\mathbf{e_{rp}}$ and the horizontal plane. The geometric relationships among $W_p$, $V_{rp}$ and $\mathbf{V_h}$ based on which equation (5) is derived are shown in Figure 5b.

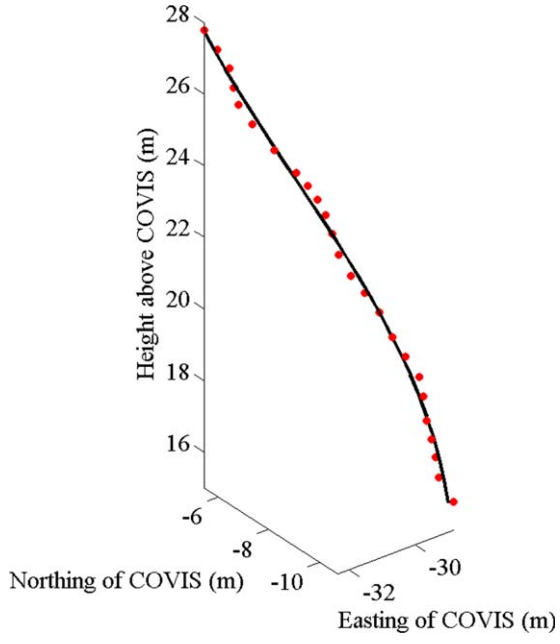


**Figure 4.** Construction of plume centerline from the 3-D gridded volume backscatter cross-section $\sigma_b$ collected on 17 October 2010. Solid line: cubic fit; red dots: $\sigma_b$ maxima on successive horizontal cross sections. Note that this figure shows a single instant of the plume centerline that varies with instantaneous ambient horizontal velocity structure over time.

## 2.3. Plume Property Estimations

[17] The plume centerline vertical velocity component $W_c$ could be obtained by substituting the measured centerline acoustic line-of-sight velocity component $V_{rc}$ and the calculated horizontal velocity $\mathbf{V_h}$ at the same altitude into equation (5). Nevertheless, it is preferable to obtain $W_c$ as the peak of the 2-D Gaussian fit applying a mathematical expression equivalent to equation (1) to the calculated plume vertical velocity distributions on successive horizontal cross sections of the 3-D grid. The averaging nature of the Gaussian-fitting process can help reduce the uncertainty in the $W_c$ estimates caused by the turbulence inside the plume and the intrinsic imprecision of the Doppler velocity measurements [*Jackson et al.*, 2003].

[18] We estimate the plume vertical volume flux $Q$ by integrating the plume vertical velocity component $W_p$ calculated using equation (5) over successive horizontal cross sections of the 3-D grid. In order to reduce the error in $W_p$ estimates caused by background noise and ambient oceanic currents, we define the boundary of the plume at $2b_\sigma$ away from the centerline, where $b_\sigma$ is the $e$-folding radius of the plume (equation (1)). We then eliminate the velocity estimates at the points where the volume backscatter cross-section $\sigma_b$ is smaller than its value at the boundary of the plume. According to equation (1), $\sigma_b$ at the boundary is approximately 2% of the $\sigma_b$ maximum. A region-growing technique is then applied to eliminate the residual velocity signals outside the plume area originating from the sporadic large $\sigma_b$ values outside the plume. It can be shown that this procedure leads to a systematic 2% underestimate of the volume flux. This bias is neglected in our uncertainty quantification as being insignificant in comparison to statistical error.

[19] The expansion rate $E_x$ (m/m) quantifies how fast a plume expands due to the entrainment of ambient seawater into the plume. Consequently, $E_x$ is a natural measure of entrainment because a plume grows faster (with larger $E_x$) under greater entrainment. In practice, we reconstruct the 2-D cross sections of the 3-D grid of the volume backscatter cross section perpendicular to the plume centerline determined in section 2.2.1. We then fit the 2-D Gaussian curve (equation (1)) to successive cross sections to obtain the $e$-folding radius $b_{\sigma\perp}$ of the plume. Finally, we determine $E_x$ by performing linear regression on the growth of $b_{\sigma\perp}$ as a function of the height above the vents,

$$b_{\sigma\perp} = E_x Z + A, \tag{6}$$

where $Z$ is the height above the vents, and $A$ is an adjustable constant.

## 2.4. Justification of Neglecting the Entrainment Inflows

[20] The geometric conversion described in section 2.2.2 neglects the inhomogeneities in the horizontal flow field inside the plume caused by the entrainment inflows $\mathbf{U_e}$. Laboratory studies indicate that $|\mathbf{U_e}|$ reaches a maximum on the plume boundary and gradually decreases to zero toward the plume centerline [*Chaengbamrung*, 2005]. Consequently, the horizontal velocity $\mathbf{V_h} = \mathbf{U_a}$ at the plume centerline and thus $\mathbf{U_e}$ has zero or negligible contribution to the plume horizontal velocity $\mathbf{V_h}$ calculated at the plume centerline. As for the flow field about the centerline, according to the entrainment hypothesis [*Morton et al.*, 1956], the magnitude of $\mathbf{U_e}$ at the boundary of the plume is proportional to the plume's centerline vertical velocity component $W_c$

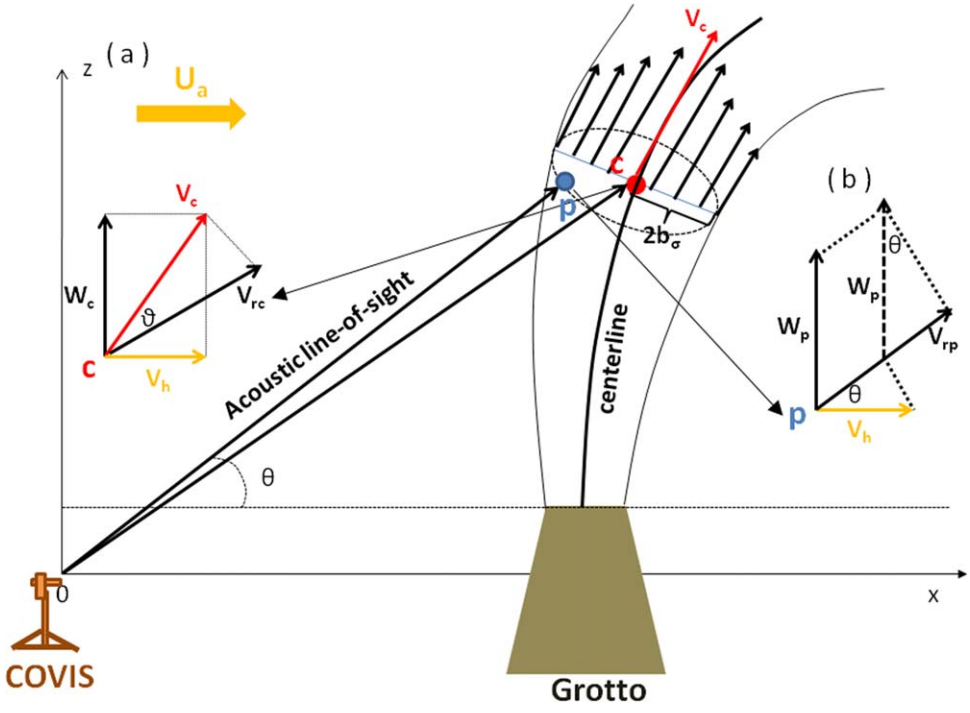


**Figure 5.** (a) Schematic diagram of the integrated plume above the North Tower of Grotto under ambient horizontal flows with plume velocities depicted on *x-z* plane for graphic convenience, which does not reflect the 3-D nature of the plume's behavior. C (red dot) is any given point located on the plume centerline at a certain altitude above Grotto. p (blue dot) is any given point at the same level of C within the plume. Velocity notations: $\mathbf{U_a}$ (thick yellow arrow), ambient horizontal flows; $\mathbf{V_c}$ (red arrow), plume velocity at C (note that $\mathbf{V_c}$ is in the axial direction according to the definition of plume centerline); $V_{rc}$, line-of-sight velocity component at C; $\mathbf{V_h}$ (yellow arrow), horizontal velocity at C; $W_c$, vertical velocity component at C; $V_{rp}$, line-of-sight velocity component at p; $W_p$, vertical velocity component at p. Note that the horizontal velocity at p is assumed to be the same as that at C (see text and supporting information S4.2). (b) Geometric relationships among $W_P$, $V_{rp}$, and $\mathbf{V_h}$.

$$|\mathbf{U_e}| = \alpha W_c, \tag{7}$$

where $\alpha$ is the entrainment coefficient. For a plume discharging into seawater with strong horizontal cross flows ($|\mathbf{U_a}| \gg W_c$), the plume is bent toward the direction of $\mathbf{U_a}$, which dominates the horizontal flow field within the plume. In such a case, $\mathbf{U_e}$ can be neglected and $\mathbf{V_h} \approx \mathbf{U_a}$ everywhere inside the plume. For a plume discharging with much greater initial velocity than the ambient flow, the plume is largely vertical as it arises from the source vents. In such a case, $\mathbf{U_e}$ dominates the horizontal flow field inside the plume and thus cannot be neglected. However, we argue that neglecting $\mathbf{U_e}$ has negligible effect on the plume volume flux estimation for the following reason.

[21] As is described in section 2.3, the plume vertical volume flux is calculated through integrating plume vertical velocity $\mathbf{W_p}$ over horizontal cross sections of the plume. According to laboratory studies [*Chaengbamrung*, 2005], $\mathbf{U_e}$ is axisymmetric and pointing perpendicularly toward the plume centerline when horizontal cross flows are negligible (in the case of vertical plumes). The error in $W_p$ induced by neglecting the contribution of $\mathbf{U_e}$ to $\mathbf{V_h}$ is also axisymmetric because of the linearity of equation (5), and is thus canceled out in the integration adopted to calculate the volume flux.

## 2.5. Uncertainty Quantification

[22] The overall uncertainties in the plume vertical volume flux $Q$ and centerline vertical velocity component $W_c$ stem from two major error sources. First, we introduce uncertainty into $Q$ and $W_c$ by using an arbitrary plume boundary at $2b_\sigma$ away from the centerline to filter the velocity estimates. In order to quantify such "arbitrariness" of the choice of the plume boundary, we allow the plume boundary to vary from $1.75b_\sigma$ to $2.25b_\sigma$ and calculate the corresponding variations in $Q$ and $W_c$. Note that the range used here is broad enough to

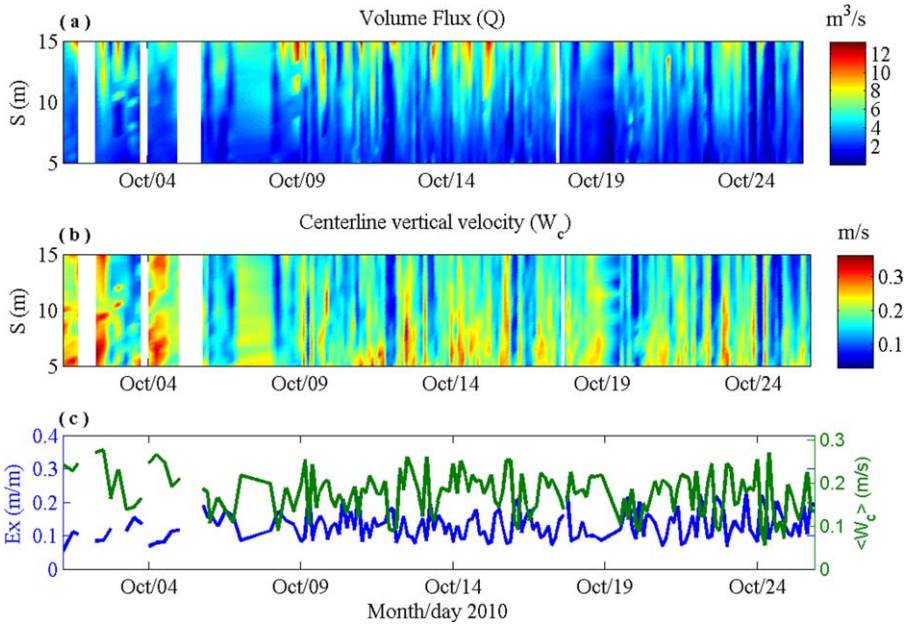


**Figure 6.** Twenty-six day time series of (a) vertical volume flux $Q$ and (b) centerline vertical velocity component $Wc$ along the axial distance range $5 < S < 15$ m for the plume above the North Tower of Grotto measured in 2010. (c) Comparison between the 26 day time series of the expansion rate $Ex$ (blue line) and the mean centerline vertical velocity component $<W_c>$ averaged over the axial distance $5 < S < 15$ m (green line). Note that the white stripes in the time series indicate no data were collected at those times.

include all the reasonable choices of plume boundaries. The results indicate the uncertainty levels are 27% in $Q$ and 6% in $W_c$ (percent of the mean value derived by using the default threshold with plume boundary defined at $2b_\sigma$ away from the centerline, blue lines in Figure 8).

[23] The second source of uncertainty is the imprecision of the Doppler measurement of line-of-sight velocity $V_r$, which propagates into $Q$ and $W_c$ through the geometric conversion and integration described in section 2.2.2 and 2.3. The total imprecision in $V_r$ estimates consists of contributions from different sources including the intrinsic error of the Doppler estimator, background noise, turbulence in the plume and ambient oceanic currents, and the bias due to finite resolution and gridding. A major, and largely unknown, source of imprecision is the turbulence in the plume. Therefore, direct quantification of the overall imprecision in $V_r$ is not feasible, and thus we use its standard deviation $V_{std}$ as a proxy (see supporting information S2) [*Jackson et al.*, 2003]. Propagating $V_{std}$ through the calculations described in section 2.2.2 and 2.3 following the rules given in *Taylor* [1982] gives the uncertainty in $Q$ and $W_c$ of 4% and 24% respectively (percent of mean, Figure 8).

## 3. Results

[24] Figure 6 summarizes the 26 day time series COVIS obtained for plume vertical volume flux $Q$, centerline vertical velocity component $W_c$, and expansion rate $E_x$ at the North Tower of Grotto in October 2010. The time series spans the beginning sector of the plume from $S = 5$ to 15 m, where S is the axial distance (distance away from the North Tower of Grotto, approximately 13 m above COVIS according to Figure 1, along the plume centerline). Here we note the key observations. Both $Q$ and $W_c$ show strong (>30%) short-term variations within the measurement period, but no distinct long-term trend (Figures 6a and 6b). The mean vertical volume flux $<Q>$ (not shown in Figure 6) averaged over the axial distance $5 < S < 15$m varies from 1.93 to 5.09 $m^3/s$. The mean centerline vertical velocity component $<W_c>$ (Figure 6c) averaged over the same axial distance varies from 0.11 to 0.24 m/s. The measured expansion rate $E_x$ $(0.082 - 0.21 m/m)$ correlates negatively with $<W_c>$ with a significant coefficient of determination $R^2 \sim 0.5$ and a $P$ value $\sim 10^{-6}$ (a $P$ value this small indicates it is extremely unlikely the correlation is an outcome of random noise). Note that the above ranges for $<Q>, <W_c>$, and $E_x$ are the

**Table 2.** Mean Values and Standard Deviations (Std) of $Q$ and $W_c$

| S (m) | $S = 5$ m | $S = 10$ m | $S = 15$ m |
|---|---|---|---|
| Mean $Q$ ($m^3/s$) | 1.88 | 3.50 | 5.83 |
| Std $Q$ ($m^3/s$) | 0.95 | 1.46 | 2.85 |
| Mean $W_c$ (m/s) | 0.21 | 0.18 | 0.16 |
| Std $W_c$ (m/s) | 0.06 | 0.06 | 0.07 |
| Std/Mean $W_c$ (Observation) | 28.6% | 33.3% | 43.8% |
| Std/Mean $W_c$ (Tidal Loading) | 11.6% | 12.5% | 12.9% |
| Tidal Loading/ Observation | 40.6% | 37.5% | 29.5% |

central 80% quantiles of their histograms (see Figure S1). Table 2 summarizes the mean values and standard deviations of $Q$ and $W_c$ at $S = 5, 10,$ and $15$ m.

[25] Our measurements of $E_x$ (average $\sim 0.14$ m/m) are consistent with the values reported in a previous study ($0.12 - 0.25$ m/m) at the same location using a different imaging sonar [*Rona et al.*, 2006]. The entrainment coefficient $\alpha$ (the constant of proportionality relating the entrainment inflows $U_e$ to the plume centerline vertical velocity component $W_c$, equation (3)) [*Morton et al.*, 1956] is a key parameter quantifying the mixing of the plume with ambient seawater. Applying the formula generalized in *Papanicolaou and List* [1988], we calculate the entrainment coefficient $\alpha$ as

$$\alpha = (5/6)E_x/1.2, \tag{8}$$

where the factor 1/1.2 is an empirical constant reflecting the assumption that the acoustic backscatter has a cross-sectional profile as dissolved tracers rather than velocity. Laboratory experiments and numerical simulations have estimated $\alpha$ for buoyant plumes in uniform or stably stratified nonflowing (horizontal cross flows $U_a = 0$) environments ($0.083 \pm 0.004$, *Fischer et al.* [1979]; 0.080 *Tao et al.* [2013], supporting information S4). These estimates fall into the lower sector of our calculated values ($0.06 - 0.14$).

[26] Figure 7 shows the smoothed, normalized periodogram of $W_c$ (see supporting information S4 for the details of the calculation of the periodogram). The periodogram has spectral peaks (with $<5\%$ significance level) centered at the frequencies consistent with the semidiurnal tidal constituents ($\sim 1.95$ cycle/day) and the local inertial oscillations ($\sim 1.5$ cycle/day).

[27] Figure 8 shows the profiles (averaged over the time series in Figures 6a and 6b) of the variations of $Q$ and $W_c$ over the axial distance range $5 < S < 15$ m. The color-shaded areas denote the uncertainty levels coming from the two error sources mentioned in section 2.5. The total uncertainty levels in the vertical volume flux $Q$ and centerline vertical velocity component $W_c$ are approximately 31% and 30% of the results obtained using the default plume boundary at $2b_\sigma$ away from the centerline respectively (blue lines in Figure 8).

## 4. Discussion

### 4.1. Advances in Data Collection

[28] To illustrate the uniqueness of the COVIS data, we briefly review the few other recent efforts

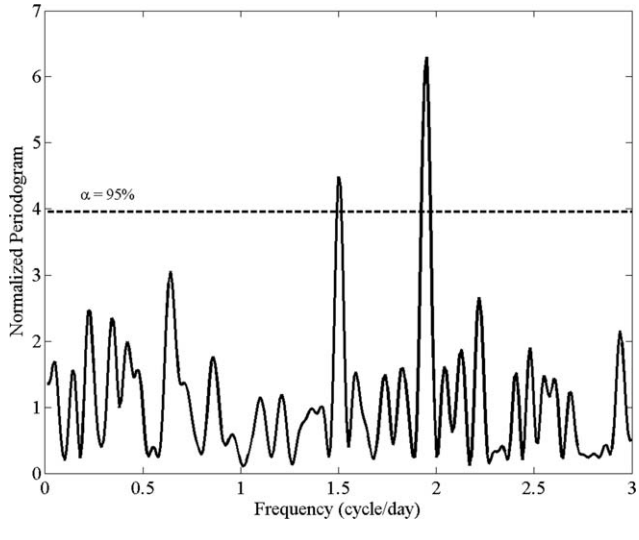


**Figure 7.** Smoothed and normalized periodogram of $W_c$ (refer to supporting information S4 for the details of the calculation of the periodogram). The dashed line denotes the 5% significance level.

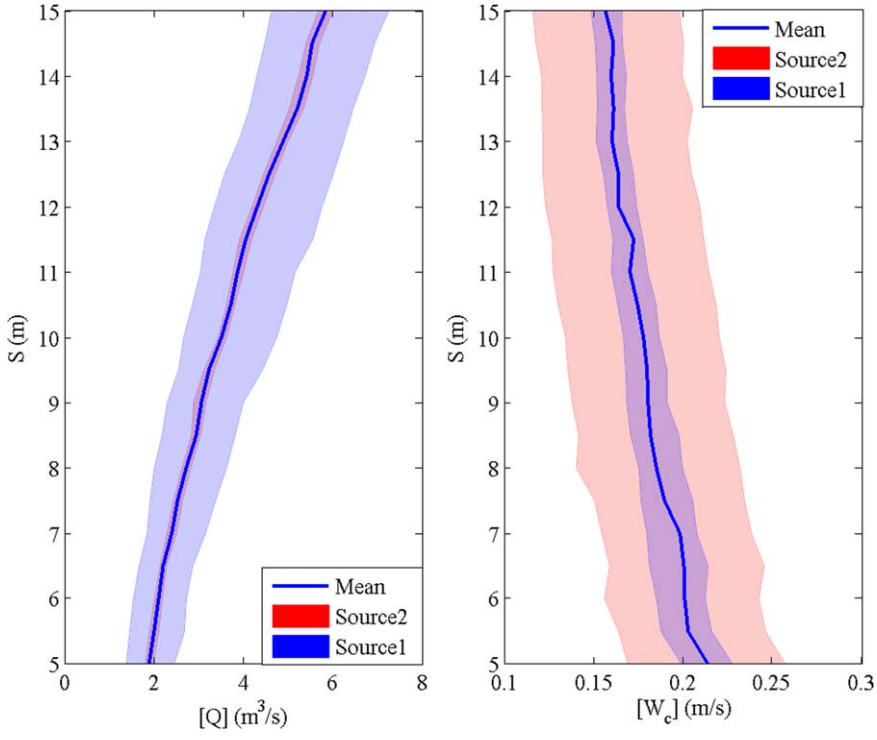


**Figure 8.** Profiles of (a) vertical volume flux [$Q$] and (b) centerline vertical velocity component [$W_c$] averaged over the 26 day time series shown in Figure 6 with uncertainties caused by the imprecision of the line-of-sight velocity measurements (source 2, red areas) and by filtering the velocity estimates with the plume boundaries defined at $1.75b_\sigma$and $2.25b_\sigma$ away from the centerline (source 1, blue areas); blue lines: mean values calculated with the plume boundary defined at $2b_\sigma$ away from the centerline (see section 2.5).

at obtaining time series of plume velocity. *Xu and DiIorio* [2012] used acoustic scintillation to obtain a 40 day time series of plume vertical velocity at 20 m above the Dante mound in MEF. Although this data set is longer, each time step only provides a single mean velocity averaged over the 20 m acoustic line-of-sight rather than the complete 3-D data set of 1-m resolution cross sections at 10 different heights provided by COVIS. *Crone et al.* [2010] collected 44 days of video of the near vent (first 2 m) region of a hydrothermal plume discharging from an individual black smoker on MilliQ vent in the MEF; they used an optical analysis technique to obtain a 44 day record of flow rate changes. While this is a longer record than that obtained by COVIS, it only measures flow from a single black smoker; as a result, extrapolation is required to infer flow through the entire sulfide mound. In contrast, the plume COVIS imaged is fed by all of the 5–10 black smokers distributed on the North Tower of Grotto; thus COVIS's flow and flux measurements reflect more directly the integrated flow through the North Tower portion of the mound.

[29] Thus, the COVIS time series of plume vertical volume flux, centerline vertical flow rate, and expansion rate represent a significant advance in data collection over earlier plume studies due to the ability to track the evolution of the plume (from ~5 to ~15 m above the vents along the centerline) and due to the confidence with which the plume is imaged (3-D resolution allows the plume to be accurately located).

## 4.2. Sources of Temporal Variations

### 4.2.1. Tidal Loading Effects

[30] In previous studies, the tidal loading effects have been reported to introduce tidal oscillations into the flow rates [*Crone et al.*, 2010] and chemical concentrations and temperatures [*Larson et al.*, 2007] of the hydrothermal plumes close to the vent orifices. These near-vent tidal oscillations can propagate downstream (vertically) and be observed at higher levels of the plumes. The variations of the temperatures measured by *Larson et al.* [2007] at high-temperature vent orifices are <6% of the mean values. The

variation in the flow rate within the beginning 2 m of the plume at a high-temperature vent measured by *Crone et al*. [2010] has a maximum ~40% of the mean value. Given the close proximity of these observations to the vent orifices, it is reasonable to consider them good approximations to the variations of the initial temperatures and flow rates of the plumes observed in the respective studies. Using the formulations described in *Morton et al*. [1956]; *Morton* [1959], we calculate the variations of the centerline vertical velocity at multiple levels (5, 10, and 15 m above the vent) of a buoyant plume caused by the initial temperature and flow-rate variations with the observed magnitudes mentioned above (see supporting information S6). The results (Tables 2 and S1) indicate the tidal loading effects can potentially cause variations in the plume centerline vertical velocity component $W_c \sim 12\%$ of the mean value, which is ~36% of the observed temporal variations. Note that these results are subject to additional uncertainty due to using the variability magnitudes observed at different vents from Grotto; however, the paucity of data gives no better idea of typical (if any) variations.

#### 4.2.2. Current-Driven Entrainment

[31] According to *Thomson et al*. [2003] and *Veirs et al*. [2006], the semidiurnal frequency dominates the tidal oscillations in the oceanic currents within the axial valley confining the Grotto mound. In addition, *Berdeal* [2006] observed significant inertial oscillations in a 11 month (June 2001 to April 2002) time series of the near-bottom (<1 m above seafloor) horizontal flows measured within the axial valley approximately 100 m to the south of the North Tower of Grotto [*Berdeal*, 2006, Figure 2.2]. The similar periodicity of the plume centerline vertical velocity component $W_c$, as is indicated by the presence of the semidiurnal (~2 cycle/day) and inertial (~1.5 cycle/day) frequencies in the spectrum (Figure 6c), is therefore a strong indicator of the plume's response to the ambient oscillatory currents.

[32] As discussed in section 2.3, the plume grows faster (with larger $E_x$) under greater entrainment. Larger measured values of $E_x$, therefore, indicate greater entrainment is occurring. Thus, the significant negative correlation between $E_x$ and the mean centerline vertical velocity component $<W_c>$ shown in Figure 6c indicates the plume rises slower under enhanced entrainment as more ambient seawater with zero or negligible vertical momentum mixes with the rising plume.

[33] According to previous laboratory and field measurements [*Fan*, 1967; *Rona et al*., 2006; *Xu and DiIorio*, 2012], ambient horizontal cross flows ($\mathbf{U_a}$) can enhance entrainment. As reported in *Thomson et al*. [2003], the currents within the southern sector of the axial valley (where Grotto is) can be decomposed as near-rectilinear tidal oscillations (~3 cm/s, sweeping back and forth along the axis of the axial valley with dominant semidiurnal constituents) superimposed on a northward mean flow (~5 cm/s). Such ambient currents enhance and introduce tidal oscillations into the entrainment at nearby hydrothermal plumes. Through the negative correlation discussed in the preceding paragraph, the tidally driven entrainment leads to the similar tidal variability (semidiurnal band) observed in the plume centerline vertical velocity component $W_c$ (Figure 7). In addition, such reasoning explains the fact that our calculated entrainment coefficients ($\alpha$) are in general larger than empirically determined values for buoyant plumes rising in nonflowing environments (section 2.3).

[34] Although the tidal loading effects discussed in the preceding section can possibly cause ~36% of the temporal variations observed in $W_c$, this theoretical estimation contradicts our observation: surface gravity waves at pure inertial frequency have zero sea-surface height variation; the sea-floor pressure, the source of the tidal loading effects, is thus free of inertial oscillations (see Figure S2 in the supporting information), which contrasts with our observations of strong inertial oscillations in $W_c$. Such a discrepancy, along with the significant negative correlation of $<W_c>$ with $E_x$, suggests the dominant source of the temporal variations in $W_c$ is the current-driven entrainment.

### 4.3. Effect of Atmospheric Forcing on Hydrothermal Vents

[35] Based on the current-driven entrainment mechanism described in the preceding section, the near-inertial peak in the spectrum (Figure 7) suggests the existence of significant inertial oscillations in the surrounding currents at Grotto during the measurement period. Atmospheric forcing, such as storms, can generate large inertial oscillations in the surface ocean. Part of the surface-generated inertial energy exits the mixing layer as internal waves that propagate downward to the deep ocean [*Thomson et al*., 1990]. Therefore, it is possible for the observed inertial oscillations to have a surface origin.

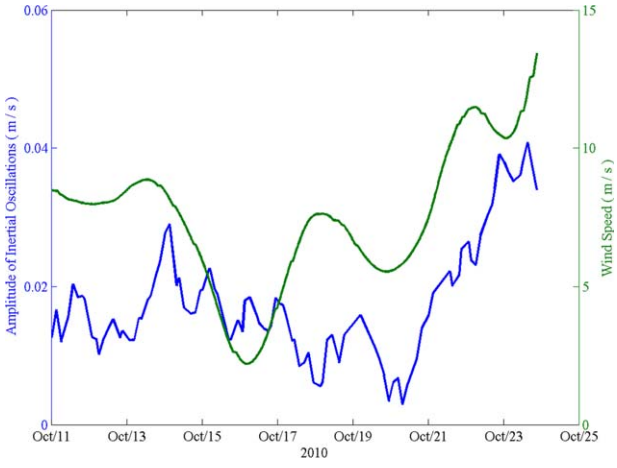


**Figure 9.** Amplitude of the inertial oscillations isolated from the mean centerline vertical velocity component $<W_c>$ shown in Figure 6c (blue) and daily averaged wind speed observed by the buoy (Station 46005, National Data Buoy Center) deployed 230 km to the south of Grotto (green).

[36] In order to investigate the relation between the observed inertial oscillations and the atmospheric forcing, we fit a sinusoidal function with the observed inertial frequency (1.5 cycle/day) to the mean centerline vertical velocity component $<W_c>$ (see supporting information S5) to isolate the inertial oscillations (Figure 6c). We then compare the amplitude of the isolated inertial oscillations with the daily averaged wind speed observed by a buoy (Station 46005, National Data Buoy Center) deployed approximately 230 km to the south of Grotto (Figure 9). The typical scale ($\sim$1000 km) of the forcing wind in the open ocean is much larger than the horizontal distance ($\sim$230 km) between Grotto and the buoy. Therefore, it is reasonable to expect high horizontal coherence between the wind fields at the two locations. The amplitude of the isolated plume inertial oscillations is significantly positively correlated with the wind speed observed by the buoy with a correlation coefficient $R \sim 0.58$ and a $P$ value $\ll 10^{-5}$.

[37] Given that the surface generated inertial energy propagates downward at the finite group velocity of internal waves, we anticipate a lag between the plume inertial oscillations and the wind speed. A cross correlation with a 13 day lag increases the correlation coefficient to $R \sim 0.69$ with a $P$ value $\ll 10^{-5}$. Assuming this time lag reflects the time taken by the internal waves to transfer the surface-generated inertial energy downward to Grotto (at 2197 m depth), the vertical group velocity of the internal waves is thus

$$C_{gz} = \frac{2197\text{m}}{13\text{days}} = 169\ \text{m/day}. \tag{9}$$

[38] According to *Kundu and Thomson* [1985], $C_{gz}$ can be calculated as

$$C_{gz} = \frac{U\left[(2\pi f)^2 - (2\pi f_0)^2\right]^{3/2}}{4\pi^2 f f_0 N}, \tag{10}$$

where $f$ is the "blue-shifted" inertial frequency observed at the bottom, $f_0$ is the original inertial frequency, $U$ is the translation speed of a storm, and $N$ is the buoyancy frequency. Substituting equation (9) along with $f_0 = 1.4851$ cycle/day, $U = 5$ m/s [*Mei et al.*, 2012] and $N = 0.001$ Hz [*Emery et al.*, 1984] into equation (10) gives $f = 1.5026$ cycle/day. This value is very close to the observed peak of the inertial band ($f \sim 1.5$ cycle/day, Figure 7) given the resolution of the spectrum $\Delta f \sim 0.06$ cycle/day.

[39] The significant correlation between the amplitude of the isolated plume inertial oscillations and the wind speed observed by the buoy, along with the consistency between the observed and calculated "blue-shifted" inertial frequencies, suggests the downward propagation of the surface-generated inertial energy into the ambient currents at Grotto. The inertial oscillations are then introduced into the plume vertical velocity component $W_c$ through the current-driven entrainment discussed in the previous section. This discovery is evidence for the influence of atmospheric forcing on the dynamics of hydrothermal plumes, which was largely overlooked in previous vent studies. Similar evidence was reported in *Adams et al.* [2011] for the influence of surface-generated mesoscale eddies on the low-frequency background currents around a hydrothermal vent field. The downward propagation of surface-generated inertial oscillations into vent fields has potential to influence the transport of hydrothermal chemical and heat fluxes and the dispersal of larvae of vent animals.

## 5. Conclusions

[40] In this paper, we use the Doppler-processed data from COVIS to measure a 26 day time series of the vertical volume flux, centerline vertical velocity component and expansion rate of the buoyant plume discharging from a hydrothermal vent cluster. We present methods of acoustic data processing and uncertainty quantification. The results

support COVIS's capability of long-term measurement of the volume flux and flow rate of a hydrothermal plume with reasonable uncertainty levels. The temporal variability of the flow rate shows frequencies of the inertial oscillations and the semidiurnal tidal constituents, which reflects the plume's response to the ambient ocean currents within the axial valley through current-driven entrainment. The observed inertial oscillations in the plume's flow rate suggest a significant influence of atmospheric forcing on the dynamics of hydrothermal plumes.

## Acknowledgments

[41] The Cabled Observatory Vent Imaging Sonar (COVIS) was customized from a commercial sonar by the Applied Physics Laboratory-University of Washington (APL-UW) in partnership with Rutgers University. Additional team members are Russ Light, Principal Engineer, Vernon Miller, Chris Jones, and Michael Kenney of APL-UW, and Deborah Silver of Rutgers University. We thank Mairi Best and Lucie Pautet, who served as cruise cochief scientists and Benoit Pirenne and their staffs in NEPTUNE Canada Data Management and Archival System (DMAS); Keith Shepherd, Keith Tamburri, and the ROV ROPOS group; David Clague, Monterey Bay Aquarium Research Institute, for bathymetry; and the National Science Foundation for support (NSF award OCE-0824612 to APL-UW; NSF award OCE-0825088 to Rutgers); anonymous reviewers and editors for the considerable efforts they put into reviewing this paper and their constructive suggestions are also acknowledged.

## References

Adams, D. K., D. J. McGillicuddy Jr, L. Zamudio, A. M. Thurnherr, X. Liang, O. Rouxel, C. R. German, and L. S. Mullineaux (2011), Surface-generated mesoscale eddies transport deep-sea products from hydrothermal vents, *Science*, *332*, 580–583, doi:10.1126/science.1201066.

Adams, D. K., S. M. Arellano, and B. Govenar (2012), Larval dispersal: Vent life in the water column, *Oceanography*, *25*, 256–268, doi:http://dx.doi.org/10.5670/oceanog.2012.24.

Anderson, R. N., and M. A. Hobart (1976), The relation between heat flow, sediment thickness and age in the Eastern Pacific, *J. Geophys. Res.*, *81*, 2968–2989.

Bemis, K. G., R. P. V. Herzen, and M. J. Mottl (1993), Geothermal heat flux from hydrothermal plumes on the Juan de Fuca Ridge, *J. Geophys. Res.*, *98*, 6351–6365.

Berdeal, I. G. (2006), Hydrography and flow in the axial valley of the endeavour segment: Implications for larval dispersal, Ph.D. thesis, Univ. of Wash., Washington, D. C.

Bickle, M., and H. Elderfield (2004), Hydrothermal fluxes in a global context, in Hydrology of the Oceanic Lithosphere, edited by E. E. Davis and H. Elderfield, pp. 677–690, Cambridge Univ. Press, Cambridge, U. K.

Chaengbamrung, A. (2005), Turbulent plumes generated by a horizontal area source of buoyancy, Ph.D. thesis, Univ. of Wollongong, New South Wales, Australia.

Chu, V. H. (1994), Lagrangian scales of jets and plumes with dominant eddies, in *Recent Research Advances in the Fluid Mechanics of Turbulent Jets and Plumes, NATO ASI Ser. E: Appl. Sci.*, vol. 255, edited by P. A. Davies and M. J. V. Neves, pp. 45–72, Kluwer Acad., Dordrecht, Netherlands.

Crone, T. J., W. S. D. Wilcock, and R. E. McDuff (2010), Flow rate perturbations in a black smoker hydrothermal vent in response to a mid-ocean ridge earthquake swarm, *Geochem. Geophys. Geosyst.*, *11*, Q03012, doi:10.1029/2009GC002926.

Emery, W. J., W. G. Lee, and L. Magaard (1984), Geographic and seasonal distributions of Brunt-Väisälä frequency and Rossby radii in the North Pacific and North Atlantic, *J. Phys. Oceanogr.*, *14*, 294–317.

Fan, L.-N. (1967), Turbulent buoyant jets into stratified or flowing ambient fluids, Tech. Rep. CaltechKHR:KH-R-15, Calif. Inst. of Technol., Pasadena, Calif.

Fischer, H. B., E. J. LIst, R. C. Koh, J. Imberger, and N. H. Brooks (1979), Mixing in Inland and Coastal Waters, Chap. 9, pp. 315–389, Acad. Press, San Diego, Calif.

Jackson, D. R., C. D. Jones, P. A. Rona, and K. G. Bemis (2003), A method for Doppler acoustic measurement of black smoker flow fields, *Geochem. Geophys. Geosyst.*, *4*(11), 1095, doi:10.1029/2003GC000509.

Jackson, P. R., J. R. Ledwell, and A. M. Thurnherr (2010), Dispersion of a tracer on the East Pacific Rise (9°N to 10°N), including the influence of hydrothermal plumes, *Deep Sea Res. Part I*, *57*, 37–52.

Kellogg, J. P., and R. E. McDuff (2010), A hydrographic transient above the Salty Dawg hydrothermal field, Endeavour segment, Juan de Fuca Ridge, *Geochem. Geophys. Geosyst.*, *11*, Q12001, doi:10.1029/2010GC003299.

Kundu, P. K., and R. E. Thomson (1985), Inertial oscillations due to a moving front, *J. Phys. Oceanogr.*, *15*, 1076–1084.

Larson, B. I., E. J. Olson, and M. D. Lilley (2007), In situ measurement of dissolved chloride in high temperature hydrothermal fluids, *Geochimi. Cosmochimi. Acta*, *71*, 2510–2523, doi:10.1016/j.gca.2007.02.013.

Mei, W., C. Pasquero, and F. Primeau (2012), The effect of translation speed upon the intensity of tropical cyclones over the tropical ocean, *Geophys. Res. Lett.*, *39*, L07801, doi:10.1029/2011GL050765.

Morton, B. R. (1959), Forced Plumes, *J. Fluid Mech.*, *5*, 151–163, doi:http://dx.doi.org/10.1017/S002211205900012X.

Morton, B. R., G. Taylor, and J. Turner (1956), Turbulent gravitational convection from maintained and instantaneous sources, *Proc. R. Soc. London*, *234*, 1–23.

Papanicolaou, P. N., and E. List (1988), Investigation of round vertical turbulent buoyant jet, *J. Fluid Mech.*, *195*, 341–391, doi:10.1017/S0022112088002447.

Rona, P. A., and D. A. Trivett (1992), Discrete and diffuse heat transfer at ASHES vent field, Axial Volcano, Juan de Fuca Ridge, *Earth Planet. Sci. Lett.*, *109*, 57–71.

Rona, P. A., K. G. Bemis, D. Silver, and C. D. Jones (2002), Acoustic imaging visualization, and quantification of buoyant hydrothermal plumes in the Ocean, *Mar. Geophys. Res.*, *23*, 147–168.

Rona, P. A., K. G. Bemis, C. D. Jones, and D. R. Jackson (2006), Entrainment and bending in a major hydrothermal plume, Main Endeavour Field, Juan de Fuca Ridge, *Geophys. Res. Lett.*, *33*, L19313, doi:10.1029/2006GL027,211.

Stein, C., and S. Stein (1994), Constraints on hydrothermal heat flux through the oceanic lithosphere from global heat flow, *J. Geophys. Res.*, *99*, 3081–3095.

Tao, Y., S. Rosswog, and M. Brug (2013), A simulation modeling approach to hydrothermal plumes and its comparison to analytical model, *Ocean Modell.*, *61*, 68–80.

Taylor, J. R. (1982), The study of uncertainties in physical measurements, in *An Introduction to Error Analysis*, Chap. 3, pp. 45–93, Univ. Sci. Books, Mill Valley, Calif.

Thomson, R. E., S. E. Roth, and J. Dymond (1990), Near-inertial motions over a mid-ocean ridge: Effects of topography and hydrothermal plumes, *J. Geophys. Res.*, *95*, 7261–7278.

Thomson, R. E., S. F. Mihaly, A. B. Rabinovich, R. E. Mcduff, S. R. Veris, and F. R. Stahr (2003), Constrained circulation at endeavour ridge facilitates colonization by vent larvae, *Nature*, *424*, 545–549, doi:10.1038/nature01824.

Thomson, R. E., M. M. Subbotina, and M. V. Anisimov (2005), Numerical simulation of hydrothermal vent-induced circulation at Endeavour Ridge, *J. Geophys. Res.*, *110*, C01004, doi:10.1029/2004JC002337.

Veirs, S. R., R. E. McDuff, and F. R. Stahr (2006), Magnitude and variance of near-bottom horizontal heat flux at the main endeavour hydrothermal vent field, *Geochem. Geophys. Geosyst.*, *7*, Q02004, doi:10.1029/2005GC000,952.

Xu, G., and D. DiIorio (2011), The relative effects of particles and turbulence on acoustic scattering from deep-sea hydrothermal vent plumes, *J. Acoust. Soc. Am.*, *130*, 1856–1867.

Xu, G., and D. DiIorio (2012), Deep sea hydrothermal plumes and their interaction with oscillatory flows, *Geochem. Geophys. Geosyst.*, *13*, Q0AJ01, doi:10.1029/2012GC004188.